UV-attenuating efficiency†

Jun Zhang,[a] Anthony P. Raphael,[b] Yannan Yang,[a] Amirali Popat,[c, d] Tarl W. Prow,[b] and Chengzhong Yu*[a]

Using a pig ear skin model, it is demonstrated that silica vesicles show higher skin safety compared to dense silica nanoparticles with similar sizes. A hydrophobic UV blocker is efficiently dispersed in silica vesicles in an amorphous state, leading to ultrahigh UV attenuating efficiency and a sun protection factor of 100 in sunscreen formulation.

Introduction

In recent years, nanomaterials have been widely used for modern pharmaceutical and cosmetic applications.[1-3] The safety of nanoparticles (NPs) is an important aspect for both scientific and public communities.[3-5] Various NPs have been investigated for their skin safety. With the protection of stratum corneum (SC), most NPs such as TiO_2 (35-250 nm), ZnO (60 nm) and Au (10-60 nm) can hardly penetrate to deep SC and epidermis.[6-8] However, skin damage from hair removal or sunburn can enhance the penetration of NPs.[6, 9, 10] With increasing topical applications of silica NPs, their skin safety has also drawn much attention. The size-dependent skin penetration behaviour of dense silica NPs has been investigated in mice[11, 12] and human skin models.[13] It is found that dense silica NPs with diameters smaller than 75 nm tend to penetrate damaged human skin, questioning their suitability in cosmetic formulations. Compared to their solid counterpart, porous silica NPs have lower density and wider applications.[1] Whilst the toxicology of silica NPs has been studied via various routes,[14] the skin safety of porous silica NPs in comparison with solid ones has not been reported.

Sunscreens are the most convenient and commonly used topical product to prevent skin damage from ultraviolet (UV) light irradiation.[15-17] Commercial sunscreens contain multiple organic UV absorbing substances (so-called blockers) as active ingredients.[18] Improvement on the dispersibility/solubility of hydrophobic UV blockers in water-based sunscreen formulations (> 60% water) is crucial for UV attenuating efficiency. For example, nanoparticulates have been prepared by micronization of crystalline organic UV blockers in sub-micron scale to enhance their efficiency.[19-21] Herzog et al. micronized 2,2'-methylenebis-(6-(2H-benzotriazol-2-yl)-4-(1,1,3,3-tetramethyl-butyl))phenol (MBBT, a broadband and hydrophobic UV blocker) crystals by a wet-milling method with the addition of surfactants. MBBT nanoparticulates (38-169 nm) show higher UV extinction, however the optimized result is still 25-33% lower than MBBT-dioxane solution. Furthermore, a fraction of UV light is scattered to skin. Li et al. reported the incorporation of crystalline benzophenone-3 in mesoporous silica aerogel, which show higher UV-attenuating efficiency than large benzophenone-3 crystals.[22] Nevertheless, 60% of the UV extinction is contributed by silica. In another example, hybrid organosilica particles were prepared by incorporating UV absorptive chromophores in the network, showing good UV absorbance compared to chromophore in true solution.[23] However, this method is not applicable to UV blockers incapable of crosslinking with silica precursors. To date, a facile method to achieve UV-attenuating efficiency of hydrophobic organic UV blockers comparable to that in true solution is still a challenge.

In the present work, two types of silica NPs have been synthesized with similar size of ~ 50 nm, including silica vesicles (SVs) with a hollow structure and solid Stöber spheres with a dense structure. Hair-removed pig ear skin is utilized as an ex vivo model for skin safety evaluation. Compared to dense Stöber spheres, it is demonstrated that SVs with a lower density are skin friendly and penetrate only in the upper part of SC (Fig. 1). It is also shown that MBBT loaded in SVs exists in an amorphous state, which exhibits superior UV-attenuating efficiency comparable to MBBT dissolved in organic solvents and a high sun protection factor (SPF) of 100 in sunscreen formulations.
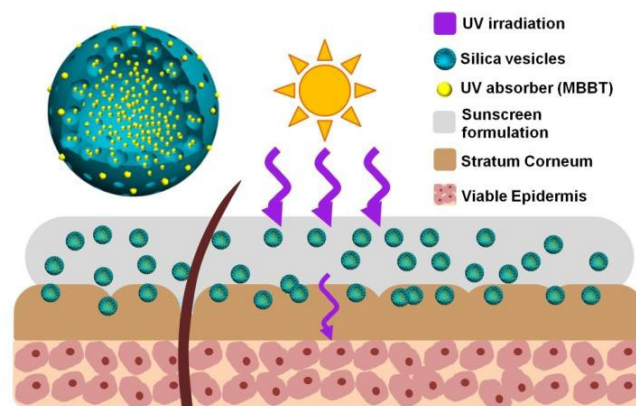
Fig.1 Schematic representation of sunscreen formulation containing nanodispersed UV blocker MBBT in skin-friendly SVs with ultrahigh UV-attenuating efficiency.

Results and Discussion

SVs were synthesized utilizing a vesicle templating method[24] while dense spheres with similar particle sizes were synthesized using Stöber method[25] (see Supporting Information, SI). Figs. 2A and C are the field-emission scanning electron microscope (FE-SEM) images of SVs and Stöber spheres, both showing a spherical morphology with a uniform particle size of ∼ 50 nm (denoted as SV-50 and SS-50, respectively). To observe the pore structure of SVs, transmission electron microscopy (TEM) was employed. SV-50 show a hollow structure with an average diamter of 45.9±3.0 nm, wall thickness of ∼ 6 nm and hollow cavity size of ∼ 34 nm (Fig. 2B). In contrast, SS-50 show a dense nature with particle size of 52.3±2.2 nm (Fig. 2D). Both SV-50 and SS-50 are negtively charged in water with the ζ potential of -16.6±0.5 and -32.8±0.6 mV, respectively (Table S1).
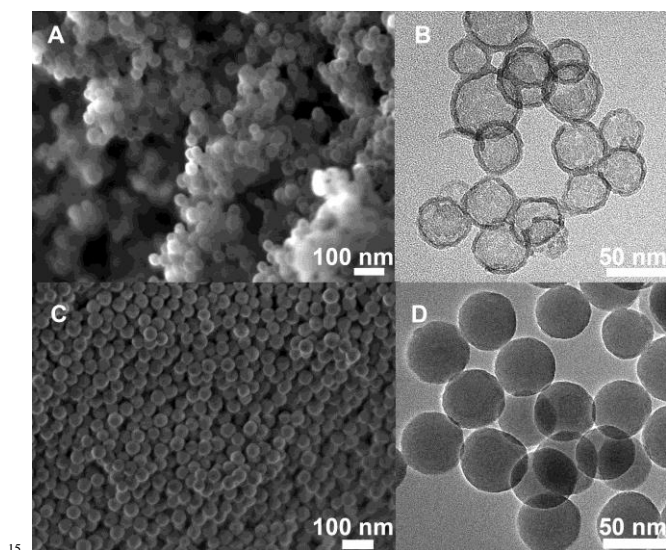

Fig.2 FE-SEM (A and C), TEM (B and D) images of calcined SV-50 and SS-50, respectively.

In order to evaluate the skin penetration of silica NPs, both SV-50 and SS-50 were modified with amino- group, after which fluorescein-5-isothiocyanate (FITC) was labelled. After conjugation of FITC, SV-50 and SS-50 show similar zeta-potential (+17.6±0.5 and +20.3±0.7 mV, respectively, Table S1) and hydrodynamic diameter (122.4 and 141.8 nm, respectively, Fig. S1). The increased sizes can be attributed to the aggregation caused by the surface modification process.[13] With similar surface chemistry and hydrodynamic size after the last FITC modification step, we further compare the difference of skin penetration behaviour between SV-50 and SS-50.

Ex vivo pig ear skin after hair removal was used as it is a suitable model for simulating human skin in sunscreen applications.[26, 27] FITC labelled silica NPs were well dispersed in water (1 mg cm^{-3}) and applied to the excised skin samples at a dose of 2 mg cm^{-2}. Confocal microscopy was used to directly observe the penetration depth of FITC modified NPs after topical application. From skin side section (Fig. 3A-C), it is observed that the penetration depth of SV-50-FITC (green fluorescence) is < 5 µm (Fig. 3A1), but much deeper (∼ 20 µm) for SS-50-FITC (Fig. 3A2). The red signal comes from skin reflectance (Fig. 3B). After merged and calibrated the depth with the skin reflectance, it is noted that SV-50 with a hollow structure mostly distribute in the upper part of SC layer (Fig. 3C1). In comparison, SS-50-FITC show a much deeper skin penetration of ∼20 µm (Fig. 3C2) which equals to the thickness of SC layer (15-20 µm), indicating that SS-50-FITC has reached the boundary between SC and viable epidermis. From the confocal images of the cross section (Fig. 3D), the strong green fluorescence with gash shape in the middle of skin indicates that the silica NPs tend to aggregate in the skin fold/furrow.
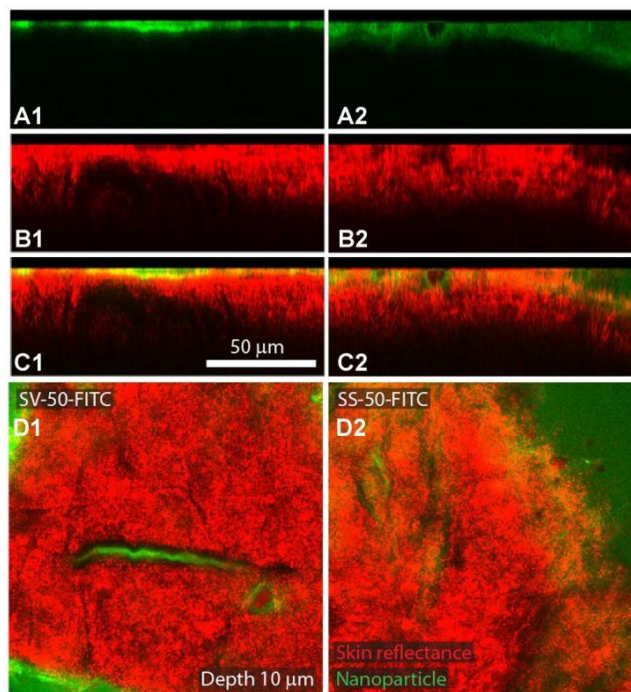
Fig.3 Confocal microscope images of *ex vivo* pig ear skin after treated with SV-50 (left) and SS-50 (right) in water suspension: (A) side section with green fluorescence from FITC-labelled NPs, (B) side section with red fluorescence from skin reflectance, (C) side section merged, and (D) cross section merged.

At the same dose of SV-50 and SS-50, different particle numbers were applied onto the skin due to their porous/solid nature. Thus, the observed difference in fluorescence may be attributed to either the particle numbers, or the nature of a hollow or solid structure. In order to elucidate this problem, the density of two particles is estimated. The density of SS-50 is chosen as that of amorphous silica (1.70 g cm^{-3}, SI, Calculation of apparent density of nanoparticles).[28] The apparent density of SV-50 is estimated using a simplified model (Fig. S2), which is 1.01 g cm^{-3}, lower than that of SS-50. The actual density of SV-50 will be even lower if the wall porosity is further considered.

The particle number applied on *ex vivo* pig skin in Figure 2 calculated from apparent density is 3.90×10^5 and 1.57×10^5 µm^{-2} for SV-50-FITC and SS-50-FITC, respectively (Table S1). Statistic skin penetration values of two particles are quantified by integrating the fluorescence density from 10 skin regions. The integrated fluorescence density normalized by particle number shows that both NPs have a decreasing distribution as a function of skin depth (Fig. S3). The integrated density of SV-50-FITC decreases from 1.99×10^{-2} (relative fluorescence unit per particle number) at the skin surface to baseline value 0.20×10^{-2} at skin depth of 5 µm. In comparison, SS-50-FITC is widely distributed in the range of 0-15 µm from the skin surface in the integrated

density from 3.06×10^{-2} to 0.29×10^{-2}, confirming that hollow SVs with a lower density indeed show lower skin penetration ability and thus higher skin safety, which is beneficial for applications in topical products. Considering the advantages including porous nature and skin friendness, SVs were chosen to encapsulate MBBT in the following tests.

A rotary evaporation method was utilized to encapsulate MBBT into SVs using MBBT-ethyl acetate (EA) solution with MBBT:SV ratio of 0.6:1, 0.8:1 and 1:1. The MBBT-SV composites are denoted MBBT-SV-X where X stands for the ratio of MBBT:SV. The actual loading amount of MBBT can be calculated by the weight loss from thermogravimetric analysis (Fig. 4A). Pure MBBT shows complete weight loss of 99.8% at 900 °C. Pure SV-50 shows 1.70% weight loss from the adsorbed moisture. The weight losses of MBBT-SV-X are 38.3, 44.9 and 50.8% for X = 0.6, 0.8 and 1.0, respectively. Accordingly, the loading amount of MBBT-SV-X (X = 0.6, 0.8 and 1.0) is calculated to be 37.3, 44.0 and 50.0%, respectively, indicating that rotary evaporation can achieve complete loading (~ 100%) of MBBT.

Figure S4A shows the Fourier transform infrared (FTIR) spectrum of pure MBBT. Eleven obvious characteristic peaks at 737, 1215, 1256, 1310, 1344, 1389, 1458, 1928, 2889, 2953 and 3068 cm^{-1} can be attributed to C-H, C-O, C-O of CH$_3$-O for phenyl, -CH$_2$-, C=C of benzene, -CH$_3$ and phenyl bonding. The spectrum of SV-50 shows a characteristic peak at 810 cm^{-1} that can be attributed to v(Si-O),[29] and broad peak in the range of 1050-1200 cm^{-1} that can be attributed to –Si-O-Si bonding.[30, 31] In the spectra of all MBBT-SV-X (C-E), besides overlapping with the characteristic peaks of silica, characteristic peaks 737, 1310, 1344, 1389, 1458, 2889 and 2953 cm^{-1} can still be observed. The FTIR spectra confirm the successful encapsulation of MBBT.

The crystalline state of MBBT before and after encapsulation is characterized by wide angle X-ray diffraction (WA-XRD, Fig. 4B). The WA-XRD pattern of pure MBBT (a) shows a sharp peak at 14.3° and other characteristic peaks in the range of 15.0-28.6°, indicating pure MBBT is in a crystalline state. SV-50 (b) shows a broad peak centred at ~ 22° which can be attributed to amorphous silica. Sharp characteristic peaks could not be observed in the WA-XRD pattern of MBBT-SV-0.6 or MBBT-SV-0.8 (c or d), indicating no crystalline MBBT is formed in these two samples. Beside the broad peak at 22°, another two broad peaks at ~ 14 and 43° are observed, attributed to MBBT. In comparison, MBBT-SV-1.0 (e) shows broad peaks at 14-20 and 43°, as well as sharp peaks (14.3, 16.2, 18.2 and 23.0°) overlapped with the broad peak from amorphous SVs. This phenomenon indicates that a fraction of crystalline MBBT exists in MBBT-SV-1.0.

The crystallization behaviour of MBBT-SV-X has also been studied by differential scanning calorimetry (DSC, Fig. 4C). Pure MBBT displays a sharp endothermic peak at 196 °C which is the melting point of crystalline MBBT.[21] Similar to pure SV-50, MBBT-SV-0.6 and MBBT-SV-0.8 show no obvious peaks in the range of 25-350 °C, indicating an amorphous state.[32] In comparison, a small endothermic peak at 196 °C is observed for MBBT-SV-1.0 as well as a physical mixture of MBBT and SVs (f), indicating the existence of crystalline MBBT structure. It is concluded that MBBT was encapsulated into SVs in a nano-dispersed form by utilizing the rotary evaporation technique.
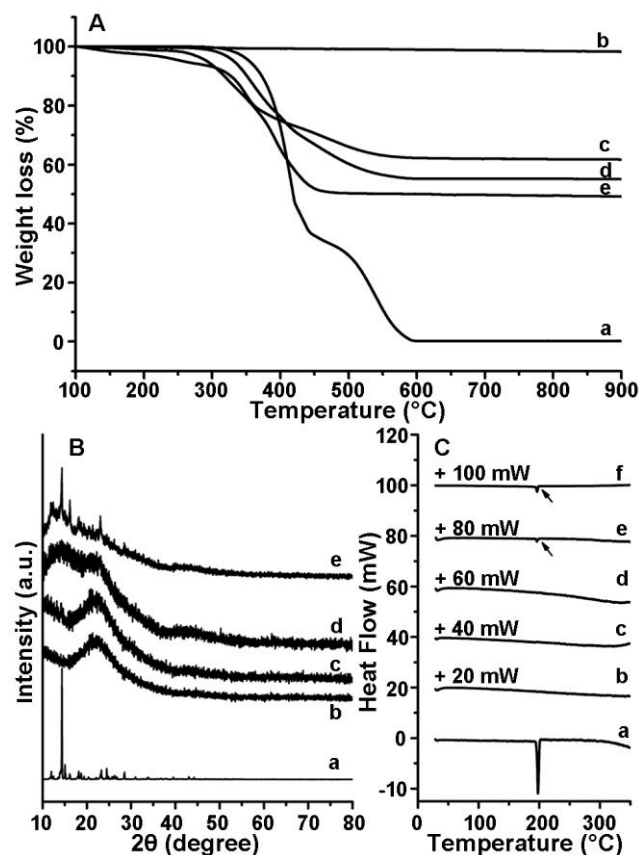
Fig.4 (A) TGA profiles, (B) wide angle XRD patterns and (C) DSC profiles of (a) pure MBBT, (b) calcined SV-50, (c) MBBT-SV-0.6, (d) MBBT-SV-0.8 and (e) MBBT-SV-1.0. (C, f) is the DSC curve for physical mixture of MBBT and SV-50.

FE-SEM was used to directly observe the morphology of MBBT-SV-X. If pure MBBT/ethyl acetate solution is used for rotary evaporation, large crystalline MBBT with the size of 1-5 μm (Fig. S5A) is formed. In the same magnification, pure SV-50 shows aggregations of small particles (B). MBBT-SV-0.6 shows exactly the same morphology as pure SV-50, and no obvious crystals of MBBT can be observed in either low (C) or high (D) magnification, indicating the MBBT is successfully encapsulated in the cavity of SVs. When the ratio of MBBT:SV increases to 1:1, small crystals (F, indicated by white arrow) appear. From nitrogen sorption analysis (Table S2), the total pore volume of SV-50 decreases from 1.22 cm^3 g^{-1} to 0.39, 0.30 and 0.26 cm^{3}g^{-1} after encapsulation of MBBT (X= 0.6, 0.8 and 1.0), respectively, indicating the mesopores of SV-50 are occupied by MBBT. Barrett–Joyner–Halanda (BJH) pore size distribution (PSD) curve of SV-50 (Fig. S6B) calculated from the adsorption branch (A) shows a peak at 39.5 nm for the cavity size. After encapsulation of MBBT, the PSD curve of MBBT-SV-0.6 shows a weak and broad peak centred at ~ 44 nm, while this peak cannot be found for MBBT-SV-0.8 or MBBT-SV-1.0, indicating the occupation of cavity by MBBT. In the case of MBBT-SV-1.0, the feeding ratio of MBBT exceed the theoretical loading capacity of SVs (SI), thus crystalline MBBT is formed outside the mesopores of SVs. The ζ potential of SV-50 after encapsulation of MBBT increases from -16.6 mV to -0.53 and -0.51 mV (MBBT-SV-0.6

and MBBT-SV-0.8, respectively), indicating a fraction of amorphous MBBT is attached on the outer surface of SV-50. For MBBT-SV-1.0 with crystalline MBBT growing outside the SV cavity, the ζ potential further increases to 0.02 mV. The hydrodynamic size of MBBT-SV-0.6 slightly increases to 141.8 nm (Fig. S8) after encapsulation.

Sunscreen formulations are preferentially water based. However, most of the organic UV blockers are hydrophobic and have very poor dispersibility/solubility and lowered UV-attenuating efficiency in water. Consequently, the addition of hazardous dispersing agent is often required.[21] With hydrophobic MBBT nanodispersed within the hydrophilic silica, MBBT-SV-0.6 can be well dispersed in water without adding any dispersing agents as demonstrated in Fig. S7A, showing the advantage of using SVs in the formulation of a pure water-based sunscreen formulation.

The UV-attenuating efficiency of MBBT solution/suspension was measured by UV-Vis spectrometry. Fig. 5 shows a series of extinction spectra calculated from direct UV-Vis transmittance (Equation S2).[21] The direct extinction is contributed by three fractions: absorbance, forward and backward scattering. Pure MBBT (green) shows no UV extinction due to the large crystal size and insolubility in water. MBBT-EA solution (0.004%, black) shows broad extinction in the range of 280-375 nm and two characteristic peaks at 304 and 346 nm for MBBT.[19, 20] In EA solution, MBBT contributes no scattering ($E_{FS} = E_{BS} = 0$). MBBT-SV-0.6/water suspension with the same concentration of MBBT (red) shows equivalent extinction to that of MBBT-EA solution, except slightly lower in the range of 333-356 nm, which is much better than MBBT prepared by other methods.[21]

The superior UV-attenuating efficiency of MBBT-SV composites should be mainly attributed to the unique nanostructure of MBBT because SVs show negligible UV extinction (Fig. S9). In the range of 360-400 nm, MBBT-SV-0.6 shows an increasing extinction contributed by UV scattering from nanodispersed MBBT.[21] In addition to MBBT, the silica structure is also important. If SVs were removed by dissolving silica in Na_2CO_3 solution (0.6 M), visible white particles can be observed in the suspension (Fig. S7B), indicating the formation of large aggregates of MBBT without the protection of siliceous shells. Such large aggregates exhibit dramatically lower UV extinction (blue curve, Fig.5). Our results indicate that the silica shell of SVs prevents the aggregation of nanodispersed MBBT and provides good water dispersity, both advantageous for the excellent UV attenuating performance in a pure water formulation.
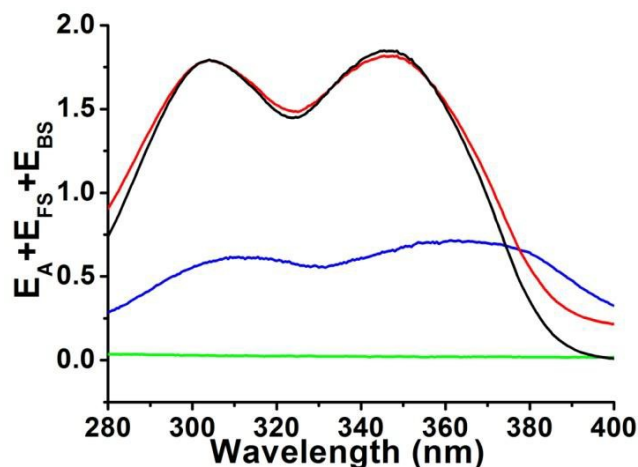
Fig.5 A series of extinction spectra calculated from direct UV-Vis transmittance of solution/suspension with MBBT concentration of 0.004% in 1 cm quartz cell, (black) MBBT in ethyl acetate solution, (red) MBBT-SV-0.6 in water suspension, (blue) MBBT-SV-0.6 in water suspension after dissolving silica by 0.6 M Na_2CO_3 solution, (green) pure MBBT in water suspension.

Although MBBT is an excellent UV blocker with broadband spectrum and scattering ability, the forward scattering of UV light towards skin is a drawback for MBBT crystals.[21] In order to evaluate the forward scattering of MBBT-SV-0.6, the diffuse extinction (absorption and backward scattering) was also calculated from the diffuse UV-Vis transmittance by Equation S3 (Fig. S10 red). By subtracting diffuse from direct extinction spectra, the contribution from forward scattering can be obtained (blue). The fraction of forward scattering of MBBT-SV-0.6 in total UV-attenuating efficiency (Fig. S11) is far lower than crystalline MBBT in submicron size.[21] It is revealed that by using amorphous MBBT nanodispersed in SVs, the UV light scattered to skin can be significantly reduced.

A cream based sunscreen formulation containing MBBT-SV-0.6 with a MBBT ratio of 1, 2, 4 and 8% has been prepared without adding dispersing agent (Table S3). The in vitro SPF value of the MBBT-SV-0.6 formulations was calculated from their diffuse transmittance[33, 34] by Equation S4. Formulations containing pure crystalline MBBT show very low in vitro SPF value of 1.22-1.86 (MBBT 1-8 w/w%). Formulations containing corresponding amount of SV-50 show in vitro SPF of 1.33-1.92. MBBT-SV-0.6 with a MBBT ratio of 1, 2, 4 and 8 w/w% show high in vitro SPF value for 2.29, 16.25, 40.71 and 100.34 in formulations, respectively. Despite the slight difference of formulation recipes, sunscreen formulations containing nanodispersed MBBT show much higher UV protection ability compared to that containing MBBT crystals with the same concentrations (Table 1).[35]

Table 1. *In vitro* SPF of formulations containing MBBT-SV-0.6.

MBBT Content (wt%)	MBBT	SV-50	MBBT-SV-0.6	Calculated SPF of MBBT[35]
1	1.23	1.33	2.29	-
2	1.22	1.33	16.25	4.9
4	1.45	1.58	40.71	6.5
8	1.86	1.92	100.34	11.3

Conclusions

In conclusion, we have demonstrated that silica vesicles with a hollow structure show higher skin safety in *ex vivo* pig ear skin compared to solid silica nanoparticles. A hydrophobic UV absorber, MBBT, has been encapsulated in silica vesicles in an amorphous state. The nanodispersed nature of MBBT confined in the cavity, the non-aggregated behaviour of MBBT protected by the siliceous shells, and the well water dipersibility of MBBT-SV composites due to the hydrophilic nature of silica all contribute to a high UV-attenuating efficiency and sun protection factor. Our findings provide fundamentally important knowledge for the design of effective and safe topical products in cosmetic and pharmaceutical applications.

Acknowledgement

Notes and references

a Australian Institute for Bioengineering and Nanotechnology, The University of Queensland, Brisbane, QLD 4072, Australia
E-mail: c.yu@uq.edu.au (C. Z. Yu)
b Dermatology Research Centre, School of Medicine, The University of Queensland, Princess Alexandra Hospital, Translational Research Institute, Brisbane, QLD 4102, Australia
c The School of Pharmacy, The University of Queensland, Brisbane, QLD 4072, Australia
d Mucosal Diseases Group, Mater Research Institute – The University of Queensland, Translational Research Institute, 37 Kent St, Woolloongabba, QLD 4102, Australia
† Electronic Supplementary Information (ESI) available: See DOI: 10.1039/b000000x/

1. Z. X. Li, J. C. Barnes, A. Bosoy, J. F. Stoddart and J. I. Zink, *Chem. Soc. Rev.*, 2012, **41**, 2590.
2. L. Zhang, F. X. Gu, J. M. Chan, A. Z. Wang, R. S. Langer and O. C. Farokhzad, *Clin. Pharmacol. Ther.*, 2008, **83**, 761.
3. A. Nel, T. Xia, L. Madler and N. Li, *Science*, 2006, **311**, 622.
4. G. Oberdorster, E. Oberdorster and J. Oberdorster, *Environ. Health Perspect.*, 2005, **113**, 823.
5. G. J. Nohynek, J. Lademann, C. Ribaud and M. S. Roberts, *Crit. Rev. Toxicol.*, 2007, **37**, 251.
6. M. Senzui, T. Tamura, K. Miura, Y. Ikarashi, Y. Watanabe and M. Fujii, *J. Toxicol. Sci.*, 2010, **35**, 107.
7. A. P. Raphael, D. Sundh, J. E. Grice, M. S. Roberts, H. P. Soyer and T. W. Prow, *Nanomedicine*, 2013, **8**, 1751.
8. D. C. Liu, A. P. Raphael, D. Sundh, J. E. Grice, H. P. Soyer, M. S. Roberts and T. W. Prow, *J. Nanomater.*, 2012, 8.
9. N. A. Monteiro-Riviere, K. Wiench, R. Landsiedel, S. Schulte, A. O. Inman and J. E. Riviere, *Toxicol. Sci.*, 2011, **123**, 264.
10. F. F. Larese, F. D'Agostin, M. Crosera, G. Adami, N. Renzi, M. Bovenzi and G. Maina, *Toxicology*, 2009, **255**, 33.
11. H. Nabeshi, T. Yoshikawa, K. Matsuyama, Y. Nakazato, K. Matsuo, A. Arimori, M. Isobe, S. Tochigi, S. Kondoh, T. Hirai, T. Akase, T. Yamashita, K. Yamashita, T. Yoshida, K. Nagano, Y. Abe, Y. Yoshioka, H. Kamada, T. Imazawa, N. Itoh, S. Nakagawa, T. Mayumi, S. Tsunoda and Y. Tsutsumi, *Biomaterials*, 2011, **32**, 2713.
12. T. Hirai, T. Yoshikawa, H. Nabeshi, T. Yoshida, T. Akase, Y. Yoshioka, N. Itoh and Y. Tsutsumi, *Pharmazie*, 2012, **67**, 742.
13. F. Rancan, Q. Gao, C. Graf, S. Troppens, S. Hadam, S. Hackbarth, C. Kembuan, U. Blume-Peytavi, E. Ruhl, J. Lademann and A. Vogt, *ACS Nano*, 2012, **6**, 6829.
14. C. H. Fu, T. L. Liu, L. L. Li, H. Y. Liu, D. Chen and F. Q. Tang, *Biomaterials*, 2013, **34**, 2565.
15. J. Y. Lin and D. E. Fisher, *Nature*, 2007, **445**, 843.
16. C. Antoniou, M. G. Kosmadaki, A. J. Stratigos and A. D. Katsambas, *J. Eur. Acad. Dermatol. Venereol.*, 2008, **22**, 1110.
17. M. R. Iannacone, M. C. B. Hughes and A. C. Green, *Photodermatol. Photoimmunol. Photomed.*, 2014, **30**, 55.
18. M. D. Palm and M. N. O'Donoghue, *Dermatol. Ther.*, 2007, **20**, 360.
19. B. Herzog, D. Huglin, E. Borsos, A. Stehlin and H. Luther, *Chimia*, 2004, **58**, 554.
20. B. Herzog, A. Katzenstein, K. Quass, A. Stehlin and H. Luther, *J. Colloid Interface Sci.*, 2004, **271**, 136.
21. B. Herzog, K. Quass, E. Schmidt, S. Muller and H. Luther, *J. Colloid Interface Sci.*, 2004, **276**, 354.
22. C. C. Li, Y. T. Chen, Y. T. Lin, S. F. Sie and Y. W. Chen-Yang, *Colloid Surf. B-Biointerfaces*, 2014, **115**, 191.
23. P. Kidsaneepoiboon, S. P. Wanichwecharungruang, T. Chooppawa, R. Deephum and T. Panyathanmaporn, *J. Mater. Chem.*, 2011, **21**, 7922.
24. J. Zhang, S. Karmakar, M. H. Yu, N. Mitter, J. Zou and C. Z. Yu, *Small*, 2014, DOI: 10.1002/smll.201401538.
25. W. Stober, A. Fink and E. Bohn, *J. Colloid Interface Sci.*, 1968, **26**, 62.
26. C. Fernandez, G. Marti-Mestres, J. Ramos and H. Maillols, *J. Pharm. Biomed. Anal.*, 2000, **24**, 155.
27. A. C. Pescia, P. Astolfi, C. Puglia, F. Bonina, R. Perrotta, B. Herzog and E. Damiani, *Int. J. Pharm.*, 2012, **427**, 217.
28. N. Husing and U. Schubert, *Angew. Chem.-Int. Edit.*, 1998, **37**, 23.
29. M. I. Tejedor-Tejedor, L. Paredes and M. A. Anderson, *Chem. Mater.*, 1998, **10**, 3410.
30. D. B. Mahadik, A. V. Rao, A. P. Rao, P. B. Wagh, S. V. Ingale and S. C. Gupta, *J. Colloid Interface Sci.*, 2011, **356**, 298.
31. Y. T. Yao, J. G. Cao, M. Yang, J. J. Li, S. Y. Zhao, W. L. Yin, Y. B. Li, X. D. He and J. S. Leng, *RSC Adv.*, 2013, **3**, 12026.
32. S. Jambhrunkar, S. Karmakar, A. Popat, M. H. Yu and C. Z. Yu, *RSC Adv.*, 2014, **4**, 709.
33. A. Springsteen, R. Yurek, M. Frazier and K. F. Carr, *Anal. Chim. Acta*, 1999, **380**, 155.
34. J. Hojerova, A. Medovcikova and M. Mikula, *Int. J. Pharm.*, 2011, **408**, 27.
35. E. Herzog, S. Mongiat, K. Quass and C. Deshayes, *J. Pharm. Sci.*, 2004, **93**, 1780.